

Unconventional superconductivity in the layered iron germanide YFe_2Ge_2

Jiasheng Chen,¹ Konstantin Semeniuk,¹ Zhuo Feng,² Pascal Reiss,¹

Yang Zou,¹ Peter W. Logg,¹ Giulio I. Lampronti,³ and F. Malte Grosche^{1,*}

¹*Cavendish Laboratory, University of Cambridge, Cambridge CB3 0HE, United Kingdom*

²*London Centre of Nanotechnology, University College London, London WC1H 0AH, United Kingdom*

³*Department of Earth Sciences, University of Cambridge, Cambridge CB2 3EQ, United Kingdom*

(Dated: June 14, 2021)

The iron-based intermetallic YFe_2Ge_2 stands out among transition metal compounds for its high Sommerfeld coefficient of the order of $100 \text{ mJ}/(\text{molK}^2)$, which signals strong electronic correlations. A new generation of high quality samples of YFe_2Ge_2 show superconducting transition anomalies below 1.8 K in thermodynamic as well as transport measurements, establishing that superconductivity is intrinsic in this layered iron compound outside the known superconducting iron pnictide or chalcogenide families. The Fermi surface geometry of YFe_2Ge_2 resembles that of KFe_2As_2 in the high pressure collapsed tetragonal phase, in which superconductivity at temperatures as high as 10 K has recently been reported, suggesting an underlying connection between the two systems.

Since the discovery of superconductivity in LaFePO [1], numerous iron-based superconductors have been identified within diverse structure families, all of which combine iron with a group-V (pnictogen) or group-VI (chalcogen) element. Unconventional superconductivity is extremely rare among transition metal compounds outside these layered iron systems and the cuprates, and it is almost universally associated with highly anisotropic electronic properties and nearly 2D Fermi surface geometries. This contrasts with the comparatively isotropic, 3D electronic structure of the iron germanide YFe_2Ge_2 [2], in which resistive and magnetic signatures of superconductivity have recently been reported [3, 4], motivating competing scenarios for the nature of the pairing mechanism [5, 6]. YFe_2Ge_2 shares key properties with the alkali metal iron arsenides $(\text{K/Rb/Cs})\text{Fe}_2\text{As}_2$: it has the same ThCr_2Si_2 structure, featuring square lattice iron layers, its low temperature heat capacity Sommerfeld coefficient is similarly enhanced, and antiferromagnetic order can be induced by chemical substitution [7]. Recent x-ray absorption and photoemission studies have demonstrated the presence of large fluctuating Fe-moments in YFe_2Ge_2 [8], suggesting that this system is close to the border of magnetism. There is an important difference, however: although YFe_2Ge_2 appears at first sight to be isoelectronic to the alkali metal iron arsenide superconductors, the existence of Ge-Ge bonds in YFe_2Ge_2 , contrasting with the absence of As-As bonds in the arsenides, causes the Fe oxidation state and consequently the electronic structure to differ from that of the arsenides.

Because initial experimental studies have failed to produce thermodynamic evidence for a bulk superconducting transition in YFe_2Ge_2 , the possibility of filamentary superconductivity from alien phases, advanced also in [9], has held back further work on this material. Here, we present transport and thermodynamic evidence for a bulk superconducting transition in YFe_2Ge_2 obtained in a new generation of high quality samples resulting from a comprehensive programme of growth optimisation. This confirms the intrinsic nature of superconduc-

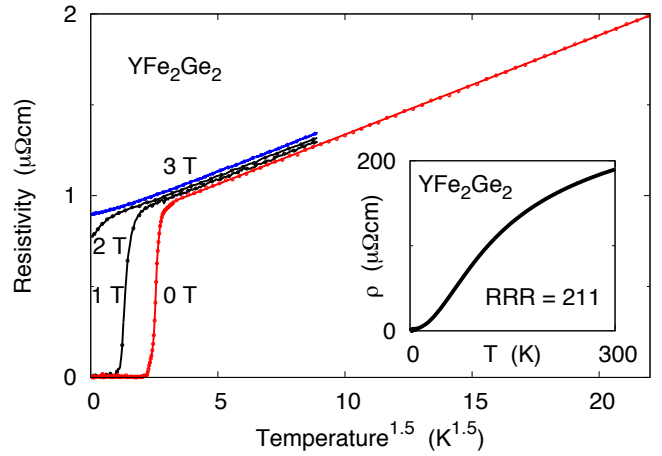


FIG. 1. Electrical resistivity of YFe_2Ge_2 versus temperature, displaying a sharp superconducting drop of the resistivity with mid-point at 1.83 K below a $T^{3/2}$ normal state temperature dependence. (inset) Temperature dependence of the resistivity up to room temperature.

tivity in YFe_2Ge_2 and motivates further investigations into the nature of its unconventional superconducting and anomalous normal state. We note, also, the striking similarity between the electronic structure of YFe_2Ge_2 and that of KFe_2As_2 in the pressure induced collapsed tetragonal state, which suggests that the two systems share a common pairing mechanism.

Polycrystalline ingots of YFe_2Ge_2 were obtained by radio frequency induction melting on a water-cooled copper boat in an argon atmosphere. To circumvent the formation of stable Y-Ge alloys, YFe_2 was first grown from the elements (Y 3N, Fe 4N). Together with elemental Ge (6N) this was then used to grow stoichiometric as well as slightly off-stoichiometric YFe_2Ge_2 . The melt was quenched and then annealed in argon at 1250°C for 1 hour, followed by further annealing in vacuum at 800°C for 8 days. More than 20 ingots with varying nominal starting compositions have been produced, reaching up

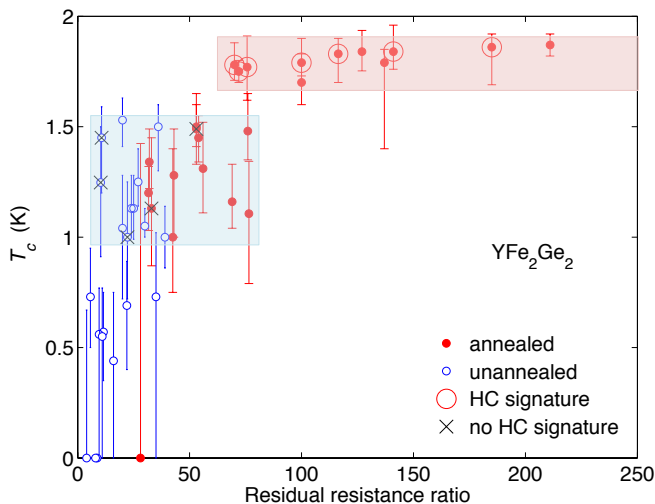


FIG. 2. Correlation between superconducting transition temperatures and residual resistance ratio $RRR = \rho(300\text{ K})/\rho(2\text{ K})$. Data points and error bars show resistive transition mid-point temperature and transition width, determined by an 80%/20% criterion. The $RRR = 211$ sample (Fig. 1) was too small for a heat capacity measurement, but the next best sample ($RRR = 185$, Fig. 3) has been extracted closely by from the same ingot. Shaded areas illustrate the step in T_c discussed in the text.

to four times higher RRR than those reported previously [3].

The electrical resistance was measured using a standard four-terminal AC technique in an adiabatic demagnetisation refrigerator to 0.1 K and in a Quantum Design Physical Properties Measurement System (PPMS) to < 0.4 K. Data were scaled at 300 K to the published high temperature resistivity [2]. The specific heat capacity was measured in a PPMS to below 0.4 K. X-ray studies [10] confirm the quality and composition of our samples. Our samples are typically 99% phase pure, and the dominant impurity phase is a ferromagnetic Fe-Ge alloy with composition approximately $\text{Fe}_{0.85}\text{Ge}_{0.15}$. The electronic structure was calculated using the Generalized Gradient Approximation [11] with Wien2k [12]. Experimentally determined lattice parameters were used for YFe_2Ge_2 and for KFe_2As_2 at ambient pressure and at a pressure of 21 GPa [13] (Tab. I). $Rk_{\text{max}} = 7.5$ and 100,000 k -points were used (6768 k -points in the irreducible Brillouin zone), and spin orbit coupling and relativistic local orbitals were included. The fractional internal position of the Ge or As layer, z , the only free internal coordinate, was optimised numerically, resulting in $z = 0.3699$ in YFe_2Ge_2 and $z = 0.3675$ in collapsed tetragonal KFe_2As_2 .

At temperatures below 10 K, the electrical resistivity of all samples of YFe_2Ge_2 displays an unconventional power-law temperature dependence of the form $\rho(T) \simeq \rho_0 + AT^{3/2}$ (Fig. 1). This suggests Fermi liquid breakdown similar to that observed in other transition

metal compounds such as MnSi , ZrZn_2 and NbFe_2 near the threshold of magnetic order [14–17] and is reminiscent of the $T^{3/2}$ power-law temperature dependences reported in early studies of KFe_2As_2 [18] and CsFe_2As_2 [19]. The dependence on residual resistivity of the resistivity exponent, which is reported to reach the Fermi liquid value of 2 in the cleanest samples of $(\text{K/Cs})\text{Fe}_2\text{As}_2$ [20], might be attributed to the hot spot/cold spot scenario for scattering from nearly critical antiferromagnetic fluctuations [21, 22].

Although most samples show resistive superconducting transitions (Fig. 1), the midpoint transition temperature T_c and the transition width depend strongly on growth conditions. The highest transition temperatures and narrowest transitions were observed in those samples which also have the highest residual resistance ratio, RRR (Fig. 2). Full resistive transitions are observed in most samples with RRR values exceeding 20, and the value of T_c , which hovers around 1.3 K up to RRR values of about 70 (blue shaded region in Fig. 2), steps up to around 1.8 K for $RRR > 70$ (red shaded region in Fig. 2). This analysis of our data does not yet take into account other underlying correlations which may affect RRR and T_c , such as slight variations in nominal stoichiometry or the effect of annealing on microscopic inhomogeneity. It does, however, suggest that the samples most likely to display bulk superconductivity may be found towards the high RRR end of Fig. 2.

Neither flux-grown samples of YFe_2Ge_2 with $RRR < 60$ nor our previous generation of induction furnace-grown samples have shown a superconducting heat capacity anomaly [3, 4]. By contrast, our new generation of samples with RRR of the order of 100 or more display clear heat capacity anomalies (Fig. 3) below the resistive transition temperature T_c . The Sommerfeld ratio, which is enhanced by an order of magnitude over the band structure value of $\simeq 10\text{ mJ}/(\text{molK}^2)$ [5, 6], rises below T_c , peaks at about 20% above the normal state value and then decreases rapidly below 0.8 K.

The superconducting heat capacity anomaly is suppressed in applied magnetic field, allowing a view of the underlying normal state. The high field data show a nearly constant Sommerfeld ratio. This suggests that the slow rise in C/T shown in [3] may actually have been the flank of a superconducting anomaly, broadened by sample inhomogeneity, although other possibilities, such as closer proximity of the earlier samples to a putative magnetic quantum critical point cannot as yet be ruled out. Using the normal state C/T measured in applied field, we can employ an entropy-conserving equal area construction to extrapolate the current data to lower temperature. Depending on the low temperature form of the heat capacity, the residual Sommerfeld coefficient in the $T = 0$ limit required by balancing the entropy reaches 24%, 42% or 53% of the normal state value, respectively, for a linear (line-nodes), quadratic (point nodes) or BCS-like (isotropic gap) temperature dependence of C/T [10].

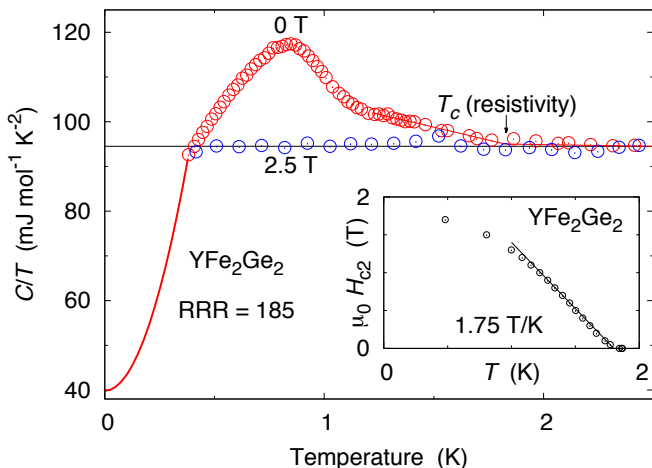


FIG. 3. C/T of YFe_2Ge_2 versus temperature. The extrapolation (red line) at low T follows a quadratic temperature dependence which matches the entropy of the superconducting state just below T_c to that of the normal state just above T_c [10]. (inset) Temperature dependence of the upper critical field determined from the mid-point of resistive transitions in the RRR = 211 sample.

Similar or even larger residual C/T fractions were found in early studies in the unconventional superconductor Sr_2RuO_4 [23], as well as in KFe_2As_2 [20] and CsFe_2As_2 [24]. SQUID magnetometry [3] suggested superconducting volume fractions approaching 80% even in samples of lower quality. It is likely that the present procedure still overestimates the residual Sommerfeld ratio. If the superconducting gap varies substantially on different sheets of the Fermi surface, as has been proposed for KFe_2As_2 [25], this can cause a marked further downturn of the heat capacity at temperatures well below T_c , not captured in the current data.

More detailed measurements to lower temperature will be necessary to distinguish between gap scenarios, but the present data already rule out alien phases as the origin of the superconducting heat capacity anomaly: powder x-ray diffraction limits alien phase content to less than 1 – 2% even in the worst cases, of which the leading contribution is made by ferromagnetic $\text{Fe}_{0.85}\text{Ge}_{0.15}$ [10]. To obtain an apparent 50% superconducting fraction from a 1% alien phase sample fraction would require the alien phase to display a colossal normal state Sommerfeld coefficient of the order of 5 J/(molK²), which would in turn not be consistent with the observed critical field, the expected composition of any alien phase and the magnitude of T_c . An anomaly of this magnitude can therefore not be consistent with the contribution of a conventional superconducting alien phase.

Further information about the superconducting state can be inferred from its response to applied magnetic field. In our new generation of samples, the initial slope of the resistive upper critical field is determined as $|dB_{c2}/dT| \simeq 1.75 \text{ T/K}$ (inset of Fig. 3). This corresponds

to an extrapolated clean-limit weak-coupling orbital-limited critical field $B_{c2}^{(o)} \simeq 0.73 T_c |dB_{c2}/dT| \simeq 2.3 \text{ T}$ [26], slightly below the value reported in [3] for a sample with a lower T_c . This discrepancy may be attributed to critical field anisotropy and preferential alignment within our polycrystals. The value for $B_{c2}^{(o)}$ exceeds the observed critical field in the low temperature limit, suggesting that the low temperature critical field is Pauli limited. In the standard treatment (e.g. [27]), the extrapolated orbital-limited critical field corresponds to a superconducting coherence length $\xi_0 = \left(\Phi_0/(2\pi B_{c2}^{(o)})\right)^{1/2} \simeq 120 \text{ \AA}$, where $\Phi_0 = h/(2e)$ is the quantum of flux. Such a short coherence length is roughly consistent with the enhanced quasiparticle mass and consequently low Fermi velocity indicated by the high Sommerfeld coefficient of the specific heat capacity: we estimate the BCS coherence length from $\xi_{BCS} = (\hbar v_F)/(\pi \Delta)$ [27, 28], where v_F is the Fermi velocity and Δ is the superconducting gap, taken to be $1.76 k_B T_c$. If the electronic structure of YFe_2Ge_2 (Fig. 4) is approximated as an ellipsoidal hole sheet around the Z point of diameter 2 \AA^{-1} and height 0.4 \AA^{-1} , its enclosed volume is $V_F \simeq 1.7 \text{ \AA}^{-3}$, corresponding to 1.1 carriers per formula unit, and its surface area $S_F^{(h)} \simeq 8.2 \text{ \AA}^{-2}$. The expression for ξ_{BCS} given above can be rewritten in terms of S_F as $\xi_{BCS} = V_0 S_F R / (1.76 \cdot 12\pi^2 \gamma_0 T_c)$, where V_0 is the volume per primitive unit cell, R is the molar gas constant and γ_0 is the normal state Sommerfeld coefficient, giving $\xi_{BCS} \simeq 166 \text{ \AA}$, in rough agreement with the estimate for ξ_0 obtained above from the critical field measurement.

The mean free path in our samples can likewise be estimated (e.g. [28]) from the Drude theory result $\ell = 6\pi^2 \hbar / (e^2 \rho_0 S_F) = 15,300 \text{ \AA} (\rho_0 / \mu\Omega\text{cm})^{-1} (S_F / \text{\AA}^{-2})^{-1}$, where S_F now includes the total Fermi surface area, which we estimate as $S_F \simeq 10 \text{ \AA}^{-2}$. This gives a mean free path of $\ell \simeq 150 \text{ \AA}$ for samples with residual resistivity $\rho_0 \simeq 10 \mu\Omega\text{cm}$ (RRR ~ 20). The observation that T_c correlates with the residual resistance ratio (Fig. 2) and that full transitions are observed in samples for which $\ell > \xi_0$ is consistent with unconventional superconductivity [29]. Heat capacity anomalies were only observed in samples with $\rho_0 < 3 \mu\Omega\text{cm}$, corresponding to $\ell > 500 \text{ \AA}$. We attribute this primarily to the consequences of sample inhomogeneity: already the magnetisation measurements [3] showed broad transitions in lower quality samples, suggesting that the resistive T_c gives an upper bound on a distribution of transition temperatures inside the sample. This distribution could be caused by inhomogeneity in chemical composition or by inhomogeneity in purity, as measured by the RRR, and it would cause the heat capacity anomaly to be smeared out in all but the best samples. Our new heat capacity data, in which the main anomaly occurs at a temperature of about 1K, well below the resistive transition, shows that even in the highest quality samples there is still a significant width to the distribution of T_c values, which would in the simplest

RFe_2X_2	a (Å)	c (Å)	c/a	X-X (Å)
YFe_2Ge_2	3.964(6)	10.457(4)	2.639	2.533
KFe_2As_2 ($p = 0$)	3.842	13.861	3.608	4.089
KFe_2As_2 (21 GPa)	3.854	9.600	2.491	2.544

TABLE I. Crystallographic parameters of YFe_2Ge_2 at ambient pressure [3], for KFe_2As_2 in the ambient pressure uncollapsed tetragonal phase [30] and in the high pressure collapsed tetragonal phase [13]. Comparing the Ge-Ge distance to the As-As distances illustrates the bond formation which accompanies the transition into the collapsed tetragonal phase.

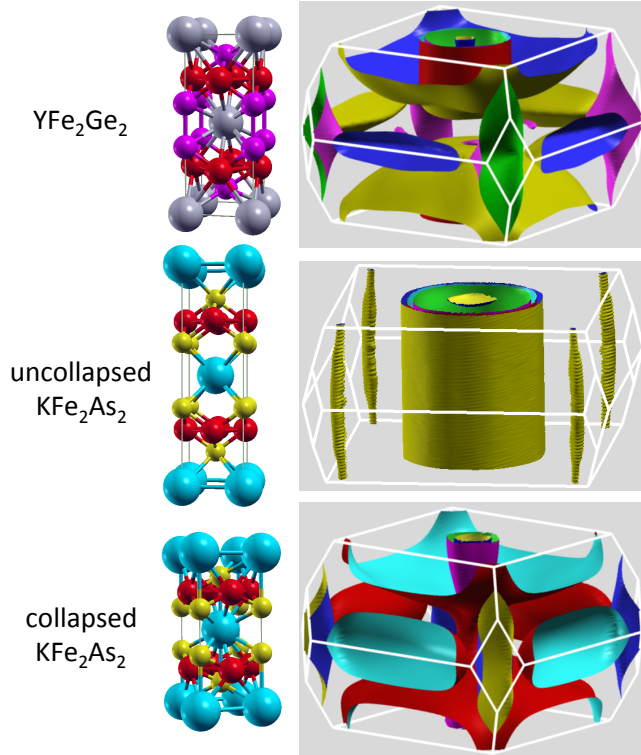


FIG. 4. Fermi surface calculated within DFT for YFe_2Ge_2 and for KFe_2As_2 in the uncollapsed (uct) and collapsed (ct) tetragonal structure. The Fermi surfaces of YFe_2Ge_2 and uct KFe_2Ge_2 are fundamentally different. Cylindrical hole sheets characterise the Fermi surface structure in uct KFe_2As_2 , whereas in YFe_2Ge_2 , nested 3D sheets around the face of the Brillouin zone (Z) and an electron pocket in the corner of the zone (X) are the main feature of the electronic structure near the Fermi energy. Conversely, the Fermi surface of ct KFe_2As_2 is strikingly similar to that of YFe_2Ge_2 .

picture follow the distribution of RRR values in the sample. Further complications could arise from multiband superconductivity.

The present thermodynamic evidence establishes superconductivity in YFe_2Ge_2 as an intrinsic bulk phenomenon, motivating a more careful look at the likely pairing mechanism. Two theoretical studies [5, 6] investigate the electronic structure of YFe_2Ge_2 , its magnetic properties and the role these could play in determining

its superconducting gap structure. Both studies arrive at a Fermi surface structure similar to that shown in Fig. 4. The Fermi surface is dominated by a large disk-shaped hole pocket enclosing the Z-point of the body-centred tetragonal Brillouin zone, as well as a cylindrical electron pocket in the corner of the zone. There are also several smaller hole pockets around the Z-point.

The calculated Fermi surface in YFe_2Ge_2 is very similar to that expected for KFe_2As_2 in the pressure induced collapsed tetragonal phase (Fig. 4) [31, 32]. This strongly suggests that YFe_2Ge_2 is an isoelectronic and isostructural reference compound to collapsed-tetragonal KFe_2As_2 . The lattice collapse in 1-2-2 arsenides is linked to the formation of As-As bonds [33] and therefore is expected to have profound consequences for the electronic structure, changing the Fe oxidation state to that of YFe_2Ge_2 , which features Ge-Ge bonds already at ambient pressure (Tab. I). In view of the recent surprising discovery of superconductivity at enhanced transition temperatures exceeding 10 K in KFe_2As_2 within the collapsed-tetragonal phase [13, 31], the scenarios for superconductivity in YFe_2Ge_2 put forward by Subedi [5] and Singh [6] assume a wider relevance. Whereas the former argues that the presence of an electron pocket at the zone corner and hole pockets near the zone centre favour antiferromagnetic spin fluctuations and an s_{\pm} order parameter wave function, the latter puts forward a more radical proposal: noting that magnetism with ordering wavevector $(0, 0, 1/2)$ can be induced in YFe_2Ge_2 by alloying with isoelectronic Lu [7, 34], and that this ordered state also represents the lowest energy spin state within DFT calculations, ferromagnetic (within the plane) correlations could induce a triplet superconducting state. The s_{\pm} scenario resembles the proposal which has been advanced for high pressure KFe_2As_2 [32].

Our experimental results demonstrate that YFe_2Ge_2 undergoes a superconducting instability at $T_c \simeq 1.8$ K out of a strongly correlated normal state with a high Sommerfeld ratio $\gamma \sim 100$ mJ/(molK²) and a non-Fermi liquid form for the temperature dependence of the resistivity, $\rho(T) \simeq \rho_0 + AT^{3/2}$. Together with the strong sensitivity to disorder of the resistive T_c and of the heat capacity anomaly this suggests an unconventional pairing mechanism. Unconventional superconductivity is rare among transition metal compounds, and YFe_2Ge_2 stands out for its comparatively isotropic, 3D Fermi surface, when compared to the cuprates, iron pnictides and chalcogenides, or Sr_2RuO_4 . The electronic structure of YFe_2Ge_2 resembles that of KFe_2As_2 in the collapsed tetragonal phase, which can be induced by applied hydrostatic pressure and in which superconductivity with transition temperatures of the order of 10 K have been reported [13, 31]. This establishes YFe_2Ge_2 as a reference compound for investigating the origin of superconductivity in the collapsed tetragonal phase in alkali metal iron arsenides, which is otherwise only accessible at very high applied pressures.

ACKNOWLEDGMENTS

We thank, in particular, S. Friedemann, M. Gamza, C. Geibel, P. Niklowitz and G. Lonzarich for helpful discussions, and J. Dann and P. Brown for assistance in aspects of sample preparation and low temperature measurement. The work was supported by the EPSRC of the UK and by Trinity College.

* fmg12@cam.ac.uk

- [1] Y. Kamihara, H. Hiramatsu, M. Hirano, R. Kawamura, H. Yanagi, T. Kamiya, and H. Hosono, *Journal of the American Chemical Society* **128**, 10012 (2006).
- [2] M. Avila, S. Bud'ko, and P. Canfield, *J. Magn. Magn. Mater.* **270**, 51 (2004).
- [3] Y. Zou, Z. Feng, P. W. Logg, J. Chen, G. Lampronti, and F. M. Grosche, *Physica Status Solidi - Rapid Research Letters* **8**, 928 (2014).
- [4] H. Kim, S. Ran, E. D. Mun, H. Hodovanets, M. A. Tanatar, R. Prozorov, S. L. Bud'ko, and P. C. Canfield, *Philosophical Magazine* **95**, 804 (2015).
- [5] A. Subedi, *Physical Review B - Condensed Matter and Materials Physics* **89**, 024504 (2014).
- [6] D. J. Singh, *Physical Review B - Condensed Matter and Materials Physics* **89**, 024505 (2014).
- [7] S. Ran, S. L. Bud'ko, and P. C. Canfield, *Philosophical Magazine* **91**, 4388 (2011).
- [8] N. Sirica, F. Bondino, S. Nappini, I. Píš, L. Poudel, A. D. Christianson, D. Mandrus, D. J. Singh, and N. Mannella, *Physical Review B* **91**, 121102 (2015).
- [9] I. Felner, B. Lv, K. Zhao, and C. W. Chu, *Journal of Superconductivity and Novel Magnetism* **28**, 1207 (2015).
- [10] See Supplemental Material at [URL] for details of the heat capacity analysis and of powder x-ray diffraction results.
- [11] J. P. Perdew, K. Burke, and M. Ernzerhof, *Physical Review Letters* **77**, 3865 (1996).
- [12] P. Blaha, K. Schwarz, G. Madsen, D. Kvasnicka, and J. Luitz, (2001).
- [13] J.-J. Ying, L.-Y. Tang, V. V. Struzhkin, H.-K. Mao, A. G. Gavriliuk, A.-F. Wang, X.-H. Chen, and X.-J. Chen, *arXiv.org* (2015), 1501.00330v1.
- [14] C. Pfleiderer, S. Julian, and G. Lonzarich, *Nature* **414**, 427 (2001).
- [15] S. Takashima, M. Nohara, H. Ueda, N. Takeshita, C. Terakura, F. Sakai, and H. Takagi, *Journal of the Physical Society of Japan* **76**, 043704 (2007).
- [16] R. P. Smith, M. Sutherland, G. G. Lonzarich, S. S. Saxena, N. Kimura, S. Takashima, M. Nohara, and H. Takagi, *Nature* **455**, 1220 (2008).
- [17] M. Brando, W. J. Duncan, D. Moroni-Klementowicz, C. Albrecht, D. Gruener, R. Ballou, and F. M. Grosche, *Physical Review Letters* **101**, 026401 (2008).
- [18] J. K. Dong, S. Y. Zhou, T. Y. Guan, H. Zhang, Y. F. Dai, X. Qiu, X. F. Wang, Y. He, X. H. Chen, and S. Y. Li, *Physical Review Letters* **104**, 087005 (2010).
- [19] X. C. Hong, X. L. Li, B. Y. Pan, L. P. He, A. F. Wang, X. G. Luo, X. H. Chen, and S. Y. Li, *Physical Review B* **87**, 144502 (2013).
- [20] F. Hardy, A. E. Böhmer, D. Aoki, P. Burger, T. Wolf, P. Schweiss, R. Heid, P. Adelman, Y. X. Yao, G. Kotliar, J. Schmalian, and C. Meingast, *Physical Review Letters* **111**, 027002 (2013).
- [21] R. Hlubina and T. M. Rice, *Physical Review B* **51**, 9253 (1995).
- [22] A. Rosch, *Physical Review Letters* **82**, 4280 (1999).
- [23] S. NishiZaki, Y. Maeno, S. Farnier, S. I. Ikeda, and T. Fujita, *Journal of the Physical Society of Japan* **67**, 560 (1998); S. NishiZaki, Y. Maeno, and Z. Mao, *Journal of Low Temperature Physics* **117**, 1581 (1999).
- [24] A. F. Wang, B. Y. Pan, X. G. Luo, F. Chen, Y. J. Yan, J. J. Ying, G. J. Ye, P. Cheng, X. C. Hong, S. Y. Li, and X. H. Chen, *Physical Review B* **87**, 214509 (2013).
- [25] F. Hardy, R. Ederl, M. Jackson, D. Aoki, C. Paulsen, T. Wolf, P. Burger, A. Böhmer, P. Schweiss, P. Adelman, R. A. Fisher, and C. Meingast, *Journal of the Physical Society of Japan* **83** (2014).
- [26] E. Helfand and N. R. Werthamer, *Physical Review* **147**, 288 (1966).
- [27] M. Tinkham, *Introduction to Superconductivity*, Vol. 1 (Dover Publications, 2004).
- [28] T. P. Orlando, E. J. McNiff, S. Foner, and M. R. Beasley, *Physical Review B* **19**, 4545 (1979).
- [29] A. Mackenzie, R. Haselwimmer, A. Tyler, G. Lonzarich, Y. Mori, S. NishiZaki, and Y. Maeno, *Physical Review Letters* **80**, 3890 (1998).
- [30] S. Rozsa and H.-U. Schuster, *Z. Naturforsch.* **36b**, 1668 (1981).
- [31] Y. Nakajima, R. Wang, T. Metz, X. Wang, L. Wang, H. Cynn, S. T. Weir, J. R. Jeffries, and J. Paglione, *Physical Review B* **91**, 060508 (2015).
- [32] D. Guterding, S. Backes, H. O. Jeschke, and R. Valentí, *Physical Review B* **91**, 140503 (2015).
- [33] R. Hoffmann and C. Zheng, *Journal of Physical Chemistry* **89**, 4175 (1985).
- [34] T. Fujiwara, N. Aso, H. Yamamoto, M. Hedo, Y. Saiga, M. Nishi, Y. Uwatoko, and K. Hirota, *Journal of the Physical Society of Japan Supplement* **76**, 60 (2007).

Superconductivity in the layered iron germanide YFe_2Ge_2 Supplemental Material

ANALYSIS OF HEAT CAPACITY MEASUREMENTS

In order to extract estimates of the low temperature residual C/T , and thereby of the non-superconducting fraction of the sample, we have extrapolated the C/T data subject to an entropy balancing constraint commonly used in this situation: the normal state entropy just above T_c has to match the entropy of the superconducting state just below T_c . To obtain the normal state entropy, we integrate up the heat capacity in applied magnetic fields larger than the upper critical field,

$$S_n(T_c) = \int_0^{T_c} \frac{C(H > H_{c2}, T)}{T} dT,$$

which can be approximated as $S_n(T_c) = \gamma_0 T_c$. Here, γ_0 is the Sommerfeld coefficient in the field-induced normal state, which is taken as constant (Fig. 5).

The superconducting state entropy has a known contribution within the measured temperature range,

$$S_1 = \int_{T_0}^{T_c} \frac{C(H=0, T)}{T} dT,$$

where T_0 is the lowest temperature measured. This integral is calculated from the measured data using the trapezoidal method. A further contribution, S_0 , then results from the extrapolation of the heat capacity data to lower temperature. It has to satisfy $S_0 + S_1 = S_n$. Moreover, we constrain the extrapolation to join the measured data point at the lowest measured temperature T_0 : $C_0(T_0) = C(H=0, T_0)$, where $C_0(T)$ is the extrapolated heat capacity.

For an initial analysis, we have chosen three forms for the temperature dependence of $C_0(T)/T$:

1. Linear, corresponding to line nodes in the gap function:

$$C_0(T)/T = \alpha_1 \gamma_0 + (1 - \alpha_1) \beta_1 T$$

2. Quadratic, corresponding to point nodes in the gap function:

$$C_0(T)/T = \alpha_2 \gamma_0 + (1 - \alpha_2) \beta_2 T^2$$

3. The BCS form for an isotropic gap Δ , which approaches $\Delta = 1.76 k_B T_c^{HC}$ in the low temperature limit, where we retain the freedom to fix a T_c^{HC} different from the resistive T_c :

$$C_0(T)/T = \alpha_3 \gamma_0 + (1 - \alpha_3) C_{BCS}(T, T_c^{HC})/T$$

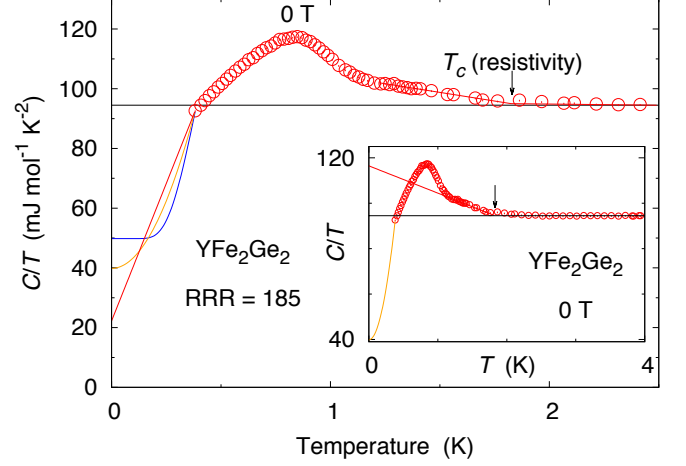


FIG. 5. Illustration of extrapolation schemes for the low temperature heat capacity in YFe_2Ge_2 . The data is the same as that shown in the manuscript. We compare a linear temperature dependence of C/T (red line), a quadratic T -dependence (orange line) and the T -dependence expected from BCS theory (blue line). The entropy of normal and superconducting states are matched at T_c , and the extrapolation function C_0 matches the measured C at the lowest measured temperature. The normal state C/T is taken from the measurement in high field shown in the manuscript, for which $C/T \simeq 94.5 \text{ mJmol}^{-1}\text{K}^{-2}$. (inset) C/T for the same sample as in the main figure, plotted over a wider T -range. The figure illustrates the distinct change in the slope of C/T vs. T near the resistive T_c .

Here, α_1 , α_2 and α_3 denote the non-superconducting fractions of the sample in the three cases. The constraints mentioned above, namely (i) matching of normal state entropy and superconducting state entropy at T_c , and (ii) matching of extrapolation function heat capacity and measured heat capacity at the lowest measured temperature T_0 , make it possible to fix α and β in the forms (1) and (2), above, or α and T_c^{HC} in the BCS form (3).

A comparison of the three extrapolation schemes is shown in Fig. 5. It demonstrates that independently of the details of the extrapolation scheme, the superconducting fraction is at least of order 50% of the sample: (i) for the linear extrapolation of C/T , $\alpha_1 = 0.24$; (ii) for the quadratic extrapolation, $\alpha_2 = 0.42$ and (iii) for the BCS form: $\alpha_3 = 0.53$. The BCS extrapolation required setting a superconducting transition temperature of $T_c^{HC} = 0.72 \text{ K}$, however, which is well below the peak in the heat capacity plot, casting doubt on its applicability.

The inset of Fig. 5 shows C/T over a wider temperature range, illustrating the change in slope in C/T vs. T near the resistive T_c . Whereas C/T is nearly constant

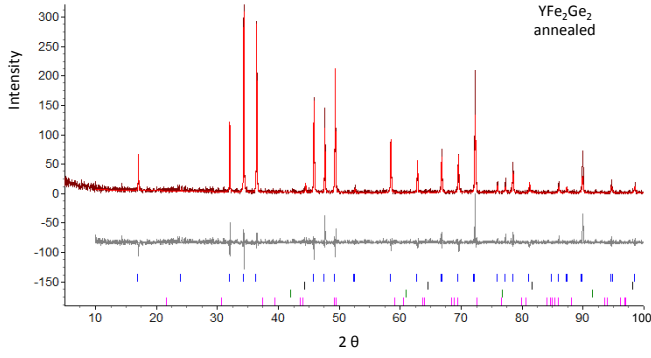


FIG. 6. X-ray pattern obtained on powder from the same annealed ingot from which the heat capacity and transport samples shown in the main part of the manuscript have been extracted. Rietveld refinement yields: (i) YFe_2Ge_2 : 98.73% (blue markers), (ii) $\text{Fe}_{0.85}\text{Ge}_{0.15}$, a bcc iron-germanium alloy with Im-3m structure: 1.16% (black markers), (iii) iron: 0.11% (green markers), and (iv) traces of FeGe_2 (I4mcm) at less than 0.01% (purple markers).

above T_c , it rises slowly below T_c (orange line on the inset in Fig. 5), before the main heat capacity anomaly is reached. The rise on cooling indicated by the orange line can be attributed to a significant fraction of the sam-

ple undergoing the superconducting transition before the main part of the sample, as would be expected from the discrepancy between the resistive T_c and the temperature at which the main heat capacity anomaly takes place.

SAMPLE CHARACTERISATION BY POWDER X-RAY DIFFRACTION

All data were collected in Bragg-Brentano geometry on a D8 Bruker diffractometer equipped with a primary Ge monochromator for $\text{Cu K}\alpha_1$ and a Sol-X solid state detector to reduce the effects of Fe fluorescence (Fig. 6). Collection conditions were: $5 - 100^\circ$ in 2θ , 0.03° step size, 10 seconds/step, divergence slits 0.1 mm, receiving slit 0.2 mm, sample spinning. Rietveld refinements were performed with the software Topas 4.1.

Crystal structures of all phases were retrieved from the inorganic crystal structure database: YFe_2Ge_2 (I4/mmm, ICSD reference code: 81745); $\text{Fe}_{0.85}\text{Ge}_{0.15}$ (Im-3m, 103493); Fe (Im-3m, 64795); FeGe_2 (I4/mcm; 42519). A spherical harmonic model was applied to correct for preferred orientation of YFe_2Ge_2 within the powder. No structural parameter was refined when resolving the phase content. A shifted Chebyshev function with six parameters was used to fit the background. Peak shapes of all phases were modelled using Pseudo-Voigt functions.